Investigation on Infrared Radiation Signatures of Under-Expanded Rocket Exhaust Plumes Due to Angle of Attack

QINGLIN NIU[ID]**1, WENQIANG GAO**[ID]**1, YIQIANG SUN**[ID]**2, AND SHIKUI DONG**[ID]**2**

[1]College of Mechatronic Engineering, North University of China, Taiyuan 030051, China
[2]Key Laboratory of Aerospace Thermophysics, Ministry of Industry and Information Technology, School of Energy Science and Engineering, Harbin Institute of Technology, Harbin 150001, China

Corresponding authors: Qinglin Niu (niuql@nuc.edu.cn) and Shikui Dong (dongsk@hit.edu.cn)

ABSTRACT A real flight trajectory varying from 5–60 km altitude was adopted for analyzing the effects of the angle of attack (AOA) on the IR signatures of rocket exhaust plumes. Three representative under-expanded states based on nozzle pressure ratio (NPR), including moderately under-expanded (NPR = 1.27), highly under-expanded (NPR = 12.5), and over-highly under-expanded (NPR = 120) states, were discussed. The results show that the appearance of the AOA shortens the plume scale size and after-burning region, but the peak temperature cannot significantly change. As an increase in the AOA, the high-temperature region and Mach cells are compressed to a small domain. The spectral radiant intensity is reduced and the decreasing rate is gradual for a large AOA. The peak radiance in the 2.7 μm band decreases, but that in the 4.3 μm band increases. The peak radiance curve shifted toward the increasing NPR as the AOA increases, and then the curve decreases monotonically from an initial "arched" shape. In addition, a group of band pairs can be observed by two intersecting in-band profiles as a function of altitude. The characteristic altitude of band pairs became more concentrated and moved toward low altitude with the increase in AOA.

INDEX TERMS Infrared signature, rocket exhaust plume, angle of attack, plume phenomenology.

I. INTRODUCTION

The rocket exhaust plume is a multi-component high-temperature supersonic free jet, which is usually rich in fuel injected from the nozzle exit [1]. After mixing with the environment, the fuel-rich exhaust burns with the oxygen of ambient air, leading to a change in the composition distribution, temperature, and radiation intensity in a certain region downstream of the nozzle exit [2]. Rocket exhaust plumes have been considered as a significant infrared radiation (IR) source and have received considerable attention in space-based detection systems for detection, tracking, classification, and identification purposes [3].

Generally, the structure of rocket exhaust plume is related to the nozzle state and flight conditions, which can be characterized by the nozzle pressure ratio (NPR) and the nozzle pressure velocity (NVR). NPR is the ratio between exit pressure of the nozzle to ambient pressure, and NVR

is the ratio between exit velocity of the nozzle to free stream velocity. According to the degree of expansion, the rocket exhaust plume can be classified into four types: low (1.0<NPR<1.1), moderately (1.1<NPR<1.2), highly (2<NPR<15), and over-highly (NPR>15) under-expanded plumes caused by the increase in flight altitude [4]. In these cases, the plume has a strong interaction with the environment and generates complex shock waves in the initial region, including expansion, compression, and reflection waves [5]. The shock waves gradually weaken as the plume develops downstream until the pressure of the plume becomes consistent with the environment. Simultaneously, afterburning occurs due to entrainment of the surrounding atmosphere and chemical reactions of oxygen in the air with unstable components of exhaust gases, such as CO, OH, and H$_2$ [6], [7], which can significantly increase the temperature of the plume. These complex physical processes also affect the electromagnetic and microwave attenuation characteristics of the rocket exhaust plume proposed by Kinefuchi *et al.* [8], [9]. The aforementioned effects depend

The associate editor coordinating the review of this manuscript and approving it for publication was Dipankar Deb[ID].

on the degree of expansion of the exhaust plume. The gaseous species and particles at high temperatures emit strong IR signatures, which has become the focus of space-based infrared detection systems [2].

Several studies on the IR signatures of rocket exhaust plumes have been conducted at a zero AOA (α, angle between thrust and vehicle velocity vector) [10]–[13]. However, the launch vehicle or missile travels with a varying AOA according to the attitude adjustment and tactical conditions [14], [15]. Generally, a moderate AOA is less than 30°, however, higher values can be employed under extreme conditions [16]. The variation in AOA changes the flow behavior, such as afterburning, shock wave, parameter distribution of species concentration, temperature, and density. In the afterburning region, respective parameters to describe the plume characteristic structure will change (see Fig. 1), including the peak temperature (T_{peak}), offset distance between the peak temperature position and the nozzle axis (D), and distance from the specified temperature position to the nozzle exit plane (L). In addition, the nozzle velocity ratio (NVR) decreases with an increase in altitude. A reduction in the relative velocity between the plume and incoming stream indicates a decreased entrainment effect. The IR signature of the plume changes as the altitude increases owing to the change in the NPR and NVR. The AOA also changes the relative velocity. These varying parameters of a plume may have a significant influence on the IR signatures [3].
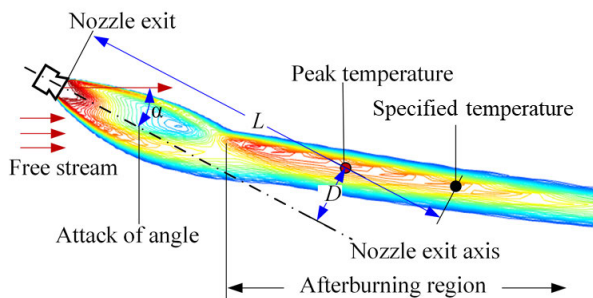

FIGURE 1. Schematic illustration of various parameters to describe the afterburning.

The significance and influence of AOA on the flows and radiation signatures have been studied sporadically in previous works. Kennedy *et al.* [16] compared and analyzed the flow field parameters of a general rocket exhaust plume at 40 km with an AOA of 15°. The study revealed that the appearance of the AOA enhanced the mixing between the plume and the ambient air, and combustion occurred early. Paiva and Slusher [3] stated that exotic spectral and spatial intensity information and asymmetric infrared thermal images may appear for space-based detection systems under the AOA case, which can be used as a phenomenology opportunity for space-based surveillance systems to finalize missile types. Simmons [2] also reported that the rocket exhaust plume phenomenology caused by the AOA could significantly change the radiation intensity and asymmetry

of the corresponding plume. In addition, some observational data for bulky launch vehicles have shown that the AOA caused a clear separate upper lobe and a stronger lower lobe fused in the trial [2], [3]. These attributes can be significant for certain defensive applications. To date, relevant studies on the influence of AOA on the IR signature of the plume are limited. Therefore, it is necessary to investigate the influence of AOA on IR signatures and rocket exhaust plume phenomenology.

In this study, the plume flow field and IR signatures are calculated through numerical methods for the liquid Atlas-IIA rocket exhaust plume. The objective of this study is to examine the influence of flight parameters on the plume radiation signature in different AOA cases, including flow field parameters, afterburning properties, infrared thermal images, spectrum, in-band radiance, and point-source band pairs. The remainder of this paper is organized as follows: Section II provides the descriptions of AOA and IR mechanisms. Section III introduces the numerical models for the plume reacting flow and IR signature. Section IV presents computation details and validation of the numerical models. Section V analyzes and discusses the influence of AOA on the plume infrared signatures. Finally, Section VI presents the concluding remarks.

II. DESCRIPTION OF PLUME AND INFRARED RADIATION PROPERTIES

For the zero AOA case ($\alpha = 0°$), the thrust vector of the motor is consistent with the incoming velocity. The plume possesses an axisymmetric structure. During the development of the plume, the supersonic flow interacts strongly with the surrounding atmosphere and produces a series of shock waves, as shown in Fig. 2. There exists a typical high-temperature core region in the downstream of the nozzle exit, where the shock wave is complex, and the Mach cells form a diamond
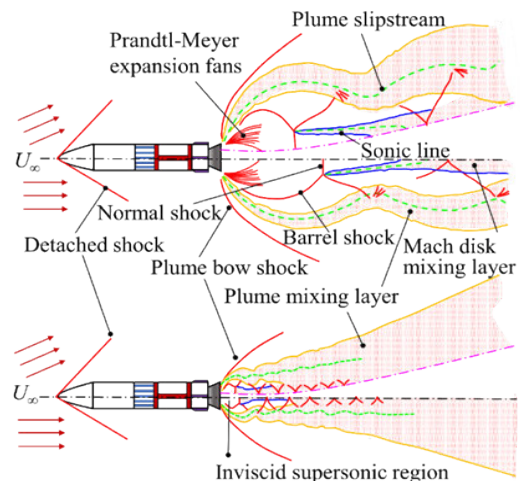

FIGURE 2. Schematic of half-section of a rocket exhaust plume for highly under-expanded (top half) and moderately under-expanded (bottom half) plumes with and without AOA, respectively.

feature in the infrared thermal radiation image. In addition, the unstable species in the mixing layer, where the plume interacts with the atmosphere, react with oxygen in the air. With the development of the plume downstream, the mixing layer gradually thickens, and the turbulence, mixing, and reacting effects are strengthened.
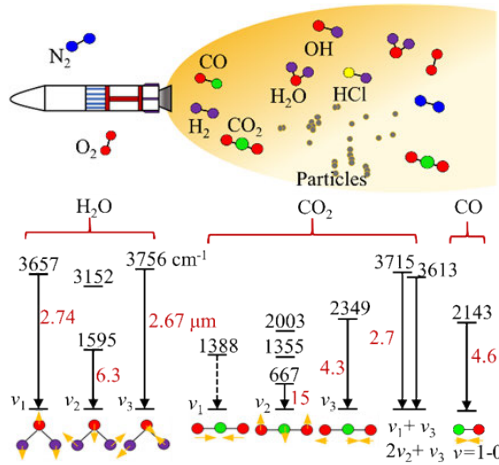

FIGURE 3. Main radiating species and their modes of vibration and energy levels for rocket exhaust plume infrared emission. The black and red Arabic numerals denote the wave number (unit: cm^{-1}) wavelength (unit: μm), respectively.

Accordingly, some factors affecting the plume IR signature also change, such as radiating species, vibrational energy levels related to temperature and number density, and spectral bands, as shown in Fig. 3. It is noted that the plume develops from the moderately under-expanded condition to an over-highly under-expanded condition with an increase in the NPR. Further, the aforementioned flow field behaviors may change with the appearance of AOA, which may possess a substantial impact on the IR signature of the plume. Therefore, the effect of AOA on the plume IR is of significant concern in engineering applications.

III. COMPUTATIONAL METHODOLOGY

A. GOVERNING EQUATIONS

The calculation of infrared radiation of rocket exhaust plume can be divided into two steps: reacting flow calculation and radiation characteristics calculation. The first step of this study is to obtain the chemical reaction flow field parameters of the plume. Previously, we have developed a FORTRAN program for simulating plume flow field, which has been successfully applied to under-expanded free jets with chemical reactions [17]. A two-dimensional infrared radiation calculation model of axisymmetric plume was established in the previous work [18], which was used for analyzing point-source infrared radiation phenomena of rocket exhaust plumes at low and middle altitudes. Based on previous work, the current calculation model needs to be extended from two-dimensional model to three-dimensional model to simulate the effect of AOA on plume.

The mass conservation for species is given by

$$\frac{\partial \rho_s}{\partial t} + \frac{\partial \rho_s u_j}{\partial x_j} = \frac{\partial}{\partial x_j}\left(\rho D_s \frac{\partial y_s}{\partial x_j}\right) + \dot{\omega}_s \quad (1)$$

where ρ_s is the density of species s (kg/m^3). $\dot{\omega}_s$ is the mass production rate (kg/(m^3·s)). u_j is the j_{th} component velocity (m/s). y_s and D_s are the mole fraction and diffusion coefficient of species s (m^2/s), respectively.

The momentum conservation is

$$\frac{\partial \rho u_i}{\partial t} + \frac{\partial \rho u_i u_j}{\partial x_j} = -\frac{\partial p}{\partial x_j} + \frac{\partial \tau_{ij}}{\partial x_j} \quad (2)$$

where p is the mixture pressure (Pa). τ_{ij} stands for the viscous stress tensor and can be written as

$$\tau_{ij} = \mu\left(\frac{\partial u_i}{\partial x_j} + \frac{\partial u_j}{\partial x_i}\right) - \frac{2}{3}\mu\frac{\partial u_k}{\partial u_k}\delta_{ij} \quad (3)$$

where μ is the viscosity of the gas mixture (N·s/m^3), and δ_{ij} is the Kronecker delta function.

The energy conservation is

$$\frac{\partial \rho E}{\partial t} + \frac{\partial \rho \tilde{H} u_j}{\partial x_j} = \frac{\partial}{\partial x_j}\left(\tilde{\eta}\frac{\partial T}{\partial x_j}\right) + \frac{\partial}{\partial x_j}\left(\rho \sum_{s=1}^{N_s} h_s D_s \frac{\partial y_s}{\partial x_j}\right)$$
$$+ \frac{\partial \tau_{ij} u_i}{\partial x_j} \quad (4)$$

where E and $\tilde{H}$ are the total energy (J/kg) and total enthalpy per unit mass of gas mixture (J/kg), respectively. T is the temperature (K) and $\tilde{\eta}$ is the thermal conductivity (W/(m·K)). h_s is the enthalpy per unit mass of species s (J/kg). For the enclosure of equations, the state equation based on Dolton's law is given by

$$p = R_u T \sum_{s=1}^{N_s} \frac{\rho_s}{W_s} \quad (5)$$

where R_u is the universal gas constant (8.314 J/(mol·K)), N_s is the number of species, and W_s is the molar weight (g/mol).

The polynomial fitting relation in Ref. [19] is used for computing the thermodynamic properties (specific heat, specific enthalpy and free energy). The transport properties (viscosity, thermal conductivity and diffusion coefficient) can be calculated by least-squares fits, and these coefficients can also be obtained in Ref. [19]. For most of the plumes, the entrainment and turbulent effects need to be considered in the mixture layer. The two-equation k-ε turbulent model is thus used in this study, which has been used in Refs. [20]–[23]. The code is based on a numerical framework finite volume method and a multi-dimensional total variation denoising (TVD) scheme to accurately simulate the supersonic flow.

B. CHEMICAL REACTION MODEL

For high-speed reacting flow, when the time of chemical reaction is comparable with the residence time of fluid element in space, the chemical reaction cannot be considered to be completed instantaneously. In this case, it is necessary

to consider the chemical non-equilibrium effect. In order to describe the chemical reaction rate of high-speed reaction flow, a finite rate chemical reaction model is used in this paper. For a single chemical reaction, the mass change rate of component s, namely the density change caused by a single chemical reaction, can be expressed as

$$\dot{\omega}_s = W_s \sum_{r=1}^{N_r} (\beta_{s,r} - \alpha_{s,r}) (R_{f,r} - R_{b,r}) \qquad (6)$$

where $\alpha_{s,r}$ and $\beta_{s,r}$ are the equivalent coefficients of reactant and product s in the rth elementary reaction, respectively $R_{f,r}$ and $R_{b,r}$ denote the formation rates of forward reaction and backward reaction in the rth reaction respectively, which have the following form

$$R_{f,r} = k_{f,r} \prod_{s=1}^{N_s} \left(10^{-3} \frac{\rho_s}{M_s} \right)^{\alpha_{s,r}} \qquad (7\text{-a})$$

$$R_{b,r} = k_{b,r} \prod_{s=1}^{N_s} \left(10^{-3} \frac{\rho_s}{M_s} \right)^{\beta_{s,r}} \qquad (7\text{-b})$$

The forward reaction rate constant $k_{f,r}$ can be determined by Arrhenius formula

$$k_{f,r} = A_{f,r} T_c^{n_{f,r}} \exp \left(\frac{E_{a,f,r}}{R_u T_c} \right) \qquad (8)$$

where A is the frequency factor, which represents the total collision frequency of the chemical reaction rate coefficient. Its unit is $(\text{m}^3/\text{mol})^{N_o-1}/\text{s}$, where N_o is the order of the reaction. E_a is the activation energy (J/mol), and T_c is the control temperature (K). The inverse reaction rate constant $k_{b,r}$ can be obtained by equilibrium constant and positive reaction rate constant. The nine-species ten-reaction chemistry reported by Wang et al. [24] was used for the flow calculations. A simplified H_2/CO reaction system with five exchange and five recombination reactions is adopted in this study. The reaction system was also used in Ref. [25].

C. INFRARED RADIATION COMPUTATION OF PLUME
The spectral band model method, which is commonly used in engineering, is used to compute the radiation of a high-temperature rocket exhaust plume. The statistical narrow band method is a single line group (SLG) model [26] based on the Curtis Godson (G-C) approximation [27] used to solve the radiation physical parameters of radiating species.

The average transmittance within a wavenumber interval has the following form

$$\bar{\tau}_\eta (L) = \exp(-\frac{\pi B}{2}(\sqrt{1 + \frac{4SL}{\pi B}} - 1)) \qquad (9)$$

where the intermediate variables are given by

$$B = 2\bar{\beta}_\eta / \pi \qquad (10\text{-a})$$
$$S = \bar{\kappa}_\eta y p \qquad (10\text{-b})$$
$$\bar{\beta}_\eta = 2\pi \bar{\gamma}_\eta / \bar{d}_\eta \qquad (10\text{-c})$$

where L is the path length (m), the subscript η denotes the wavenumber (cm^{-1}). $\bar{\gamma}_\eta$, $\bar{d}_\eta$ and $\bar{\kappa}_\eta$ are the average band model parameters, which stand for the half-width at half-maximum (HWHM), the band spacing, and the absorption coefficient, respectively. The required parameters are obtained from the NASA-SP-3080 database [26]. The database provides the radiative parameters of the main molecules (such as CO_2, H_2O, CO, HCl, NO, OH, etc.) within the temperature range of 300-3000 K.

For propellants without considering the influence of metal additives, the radiative transfer equation does not involve particle scattering. Therefore, the spectral radiation intensity along a specific path can be conveniently solved by the following expression

$$I_\eta = -\int_0^L I_{b\eta} (T) \frac{d (\tau_\eta)}{dl} dl \qquad (11)$$

where I_η is the emitting spectral radiation intensity (W/(sr·m^2·cm^{-1})), and $I_{b\eta}(T)$ is the local blackbody spectral radiation (W/(sr·m^2·cm^{-1})). τ_η is the local transmission along the integral path. At a fixed observation angle, the radiation intensity along the path is obtained using the line-of-sight (LOS) clusters passing through the plume inclusion. The infrared thermal image of the plume can be easily obtained by integrating the spectral bands. A detailed algorithm can be found in Ref. [17].

IV. DESIGN OF NUMERICAL EXPERIMENT AND COMPUTATION DETAILS
A. GEOMETRY AND MESH SIZE
The Atlas-IIA rocket has a multi-nozzle kerosene/liquid oxygen motor group, which consists of one main and two booster motors [28]. The detailed configuration and geometry size are provided in Ref. [28]. To study the flow field and IR signatures of the Atlas-IIA plume, various studies [29], [30] adopted an equivalent single nozzle to characterize the multinozzle structure. Hence, the nozzle exit parameters of a single nozzle can be calculated according to the equivalent principle of the flow rate and species mass flow. However, the multi-nozzle has a proper effect on the flow field structure and radiation signatures. Generally, the structure of a typical missile body is composed of a blunt cone and a section of a cylindrical structure. In this study, we intend to examine the effect of AOA on the radiation signature of plume. Therefore, the multi-nozzle effect is not considered. A three-dimensional model is used for the AOA cases. To reduce the computation cost, a half model is used, as shown in Fig. 4(a) and (b).

In simulation, an appropriate mesh size and distribution is necessary to satisfy all calculation cases, specifically for large AOA cases. Accordingly, the calculation domain adopts a half cylinder having 2000 m length and 300 m radius, and the mesh distribution is shown in Fig. 4(b). The computational mesh has 700 × 120 points in the streamwise and radical directions with 50 transverse points, respectively. The mesh is refined at the nozzle exit and base regions, and also extends

TABLE 1. Exit conditions of the equivalent single nozzle.

Fluid conditions			Mass fraction of species						
T_e, K	P_e, Pa	U_e, m/s	H_2	H_2O	O_2	H	OH	CO	CO_2
2230	68850	2960	0.012194	27.2437	0.000028	0.000127	0.000797	0.412125	0.302293

(a) Schematic diagram of calculation domain

(b) Mesh distribution
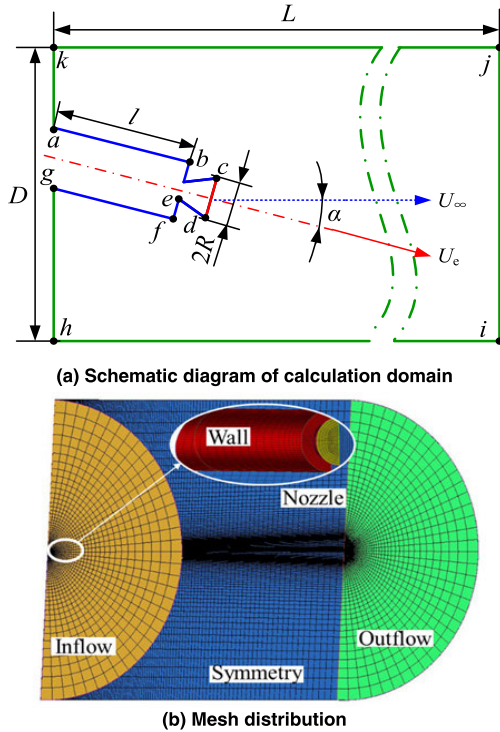
FIGURE 4. Computational model of a general rocket exhaust plume with an equivalent single nozzle.

toward the exit of the computational domain along the region where the plume passes.

B. BOUNDARY CONDITIONS

The distribution estimation of the flow field parameters, including pressure, temperature, and species number density is a prerequisite for the computation of IR signatures. The high-temperature shock layer of the fore body also has a certain effect on the IR of the plume. For simplification, only the effect of AOA on plume radiation signatures is considered in this study.

According to the calculation domain shown in Fig. 4(a), the following boundary conditions are employed: A non-slip, constant-temperature wall is applied to the body (*a-b-c* and *d-f-g*) and the nozzle surface (*c-d*). A multi-species velocity and temperature boundary condition is used on the nozzle exit plane, as shown in Table 1. Uniform co-flowing conditions are specified at the entrance (*g-h* and *a-k*) and far-field boundaries (*k-j* and *h-i*) of the computational domain. The incoming flow parameters including the flight speed, ambient pressure, and temperature, depend on the flight trajectory of the vehicle as discussed in Section IV-C. The exit boundary (*i-j*) is considered as a supersonic boundary and obtained by extrapolation of the upstream parameters.

C. COMPUTATIONAL CASES

Usually, the speed of the launch vehicle and the ballistic missile increases with an increase in flight altitude during the boost phase. The structure and parameter distribution of plume depend on the flight speed and altitude. The NVR is related to the entrainment effect of the environment, which affects the air mixing and afterburning. With the increase in NPR, the density of the atmospheric environment decreases with an expansion in rocket exhaust plume, and the mixing effect of oxygen declines simultaneously.

In this study, seven cases of AOA ranging between 0° to 30° with a constant interval of 5° are considered. The flight altitude includes 12 cases, ranging between 5 km to 60 km with a constant interval of 5 km. The flight altitude is obtained from the real trajectory of Atlas-IIA at a flight time segment ranging between 58–161 s [31]. The flight Mach number ranges from 0.71 to 7.80. The range of NPR is significantly wide, spanning three orders of magnitude, from 10^0 to 10^3. This indicates that the exhaust plume experienced three types of under expansion: moderately, highly, and over-highly under-expanded conditions. The NVR values ranging between 1.2–13 are considered. Fig. 5 shows the variation in flight altitude and Mach number curves with NVR and NPR. From Fig. 5, it is evident that the flight altitude and speed are closely related. In summary, there are 84 plume flow field calculation cases in this study. The co-flowing parameters at zero AOA are listed in Table 2. The velocity at other AOAs is calculated using the component of velocity at $\alpha = 0°$.
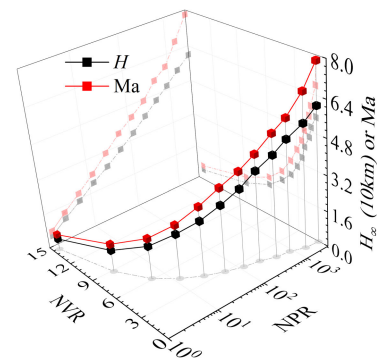

FIGURE 5. Profiles of altitude (*H*) and Mach number (Ma) with NPR and NVR.

D. VALIDATION OF MODELS

The liquid Atlas-IIA rockets launched from the Kennedy Space Center on the night of May 3, 2000, were observed by the Ballistic Missile Defense Operations (BMDO) Innovative Science and Technology Experiment Facility (ISTEF) and
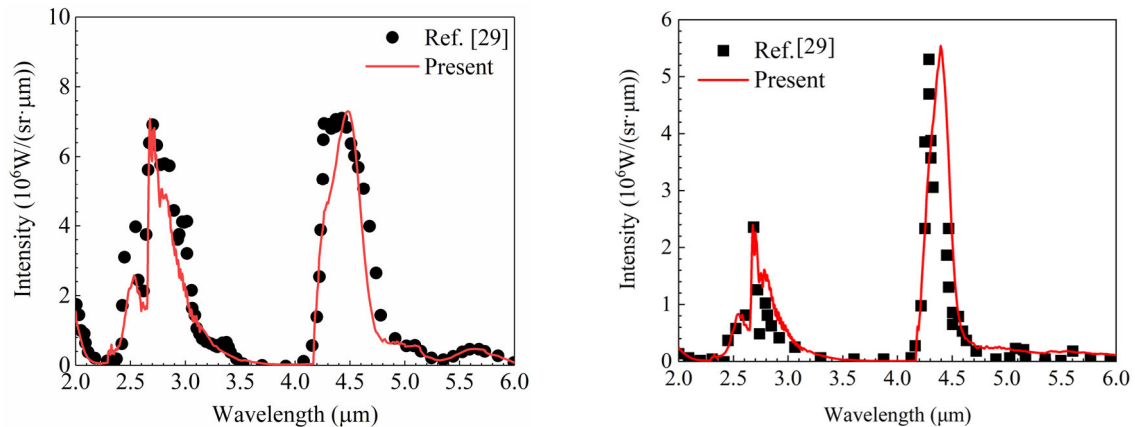
FIGURE 6. IR intensity of the Atlas-IIA rocket exhaust plumes for (a) 21 km and (b) 41 km.

TABLE 2. Freestream conditions of ATLAS-II at $\alpha = 0°$.

t, s	U_∞, m/s	H_∞, km	P_∞, kPa	T_∞, K	Ma
58	226.2	5	54.048	255.7	0.71
76	382.0	10	26.500	223.3	1.28
90	545.5	15	12.112	216.7	1.85
102	720.1	20	5.529	216.7	2.44
113	930.0	25	2.549	221.6	3.12
122	1131.4	30	1.197	226.5	3.75
128	1308.5	35	0.575	236.5	4.24
135	1504.6	40	0.287	250.4	4.74
143	1771.9	45	0.149	264.2	5.44
148	1934.5	50	0.080	270.7	5.87
155	2202.9	55	0.043	260.8	6.80
161	2456.1	60	0.022	247.0	7.80

the Arnold Engineering Development Center (AEDC) [32]. These data have been used to validate the numerical models. Considering the numerous conditions involved in the observation data, several studies have adopted the equivalent single nozzle model, as discussed in Section IV-B.

Ozawa *et al.* [29] calculated the radiation spectra of the Atlas-IIA plume with an equivalent nozzle at altitudes of 21 km and 41 km for $\alpha = 0°$ using the nonequilibrium radiation distribution (NERD) program. In this test case, the axial and radial dimensions of the computational domain are 100 m and 30 m, respectively, and the boundary conditions are the same as those described in Section IV-B. Further, the observation angle is perpendicular to the plume axis. It is to be noted that the computing results are the spectrum of the self-emission intensity of the plume. More detailed information can be found in Ref. [29]. In the current calculation, the spectral resolution is 5 cm^{-1}. Fig. 6 shows the comparison of the radiation spectrum between the calculated values and the reference data in the 2.0–6.0 μm band. It can be seen that the simulation results are in good agreement with reference results, except for some underestimation in the wavelength band of 2.3–2.5 μm. In addition, our previous work [17] also gave the detailed process of validating the calculation model by using the infrared measurement data of the ground test of the exhaust plume.

V. RESULTS AND DISCUSSIONS

A. EFFECT OF AOA ON FLOW FIELD PROPERTIES

High-temperature exhaust gas is injected into the atmosphere from the nozzle exit, which has a strong interaction with the environment and produces complex shock waves at the origin. The shock waves gradually weaken as the plume develops downstream until the pressure of the plume becomes consistent with the environment. The exhaust plume mixes with the surrounding atmosphere and entrains oxygen in the air to participate in the chemical reaction of the unstable components. A shear layer is formed by the interaction between the exhaust plume and the environment, and subsequently the temperature of the exhaust plume increases with the occurrence of afterburning.

Fig. 7 shows the temperature distributions of the three types of under-expanded plumes at the three representative AOAs. Each illustration from top to bottom shows the temperature distribution on the symmetry plane of the plume at $\alpha = 0°$, 15° and 30°, respectively. It can be seen from Fig. 7(a) that the moderately under-expanded plume (NPR = 1.27) forms typical Mach cells near the nozzle exit region (also shown in Fig. 2). In a certain downstream region, the temperature is lower than that of the nozzle exit. Subsequently, the temperature and its range increase close to the nozzle exit temperature. The apparent afterburning region disappears at $\alpha = 15°$ owing to the existence of AOA. The AOA causes the incoming flow to interact with the exhaust plume, which is similar to the appearance of the windward side, compressing the exhaust plume into a limited area with a slender shape. With an increase in the AOA, the high-temperature region of the plume decreases, and the Mach cells are compressed to a small domain. In this case, the flow field structure is still relatively smooth. For the highly under-expanded plume (NPR = 12.5) shown in Fig. 7(b), the Mach cell disappears near the nozzle exit, and the initial shock structure change results in formation of a Mach disk. The temperature is also lower than that of the nozzle exit. An evident afterburning phenomenon occurred in the downstream region of the plume. It should be noted that the core region of the plume near the
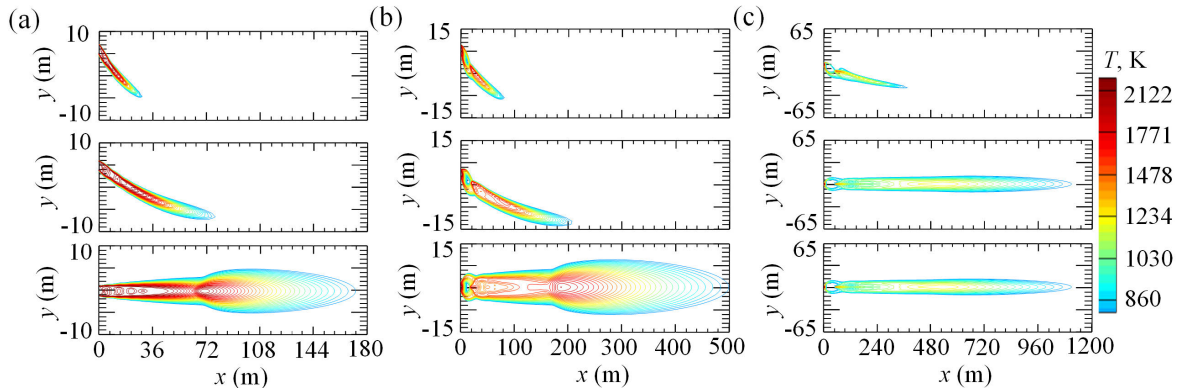
FIGURE 7. Temperature contours on symmetry plane of the plume for different AOA cases. The illustrations are $\alpha = 0°$, $\alpha = 15°$, and $\alpha = 30°$ from bottom to top; (a) NPR = 1.27 (moderately under-expanded state), (b) NPR = 12.5 (highly under-expanded state), and (c) NPR = 120 (over-highly under-expanded state).
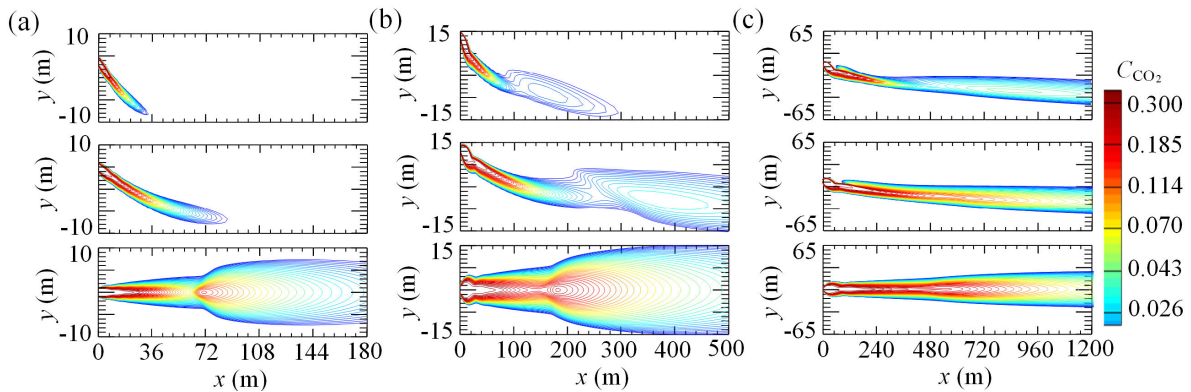

FIGURE 8. Contours of CO_2 mass fraction on symmetry plane of the plume for different AOA cases. The illustrations are $\alpha = 0°$, $\alpha = 15°$, and $\alpha = 30°$ from bottom to top; (a) NPR = 1.27 (moderately under-expanded state), (b) NPR = 12.5 (highly under-expanded state), and (c) NPR = 120 (over-highly under-expanded state).

nozzle exit is severely deformed owing to the AOA, which changes the temperature and its distribution. The over-highly under-expanded plumes (NPR = 120) are shown in Fig. 7(c), where the position of the Mach disk is far away from the nozzle exit, resulting in a decreased overall plume temperature. The high-temperature region primarily exists in the afterburning region. With an increase in the AOA, the deformation in the expansion area of the plume appears as a small high-temperature region.

Fig. 8 shows the mass fraction distributions of CO_2. The distribution structure of the CO_2 mass fraction is similar to that of temperature. The size range of CO_2 is smaller than that of temperature, which is due to the fact that the temperature generation lags behind the chemical reaction with the development of flow field. The CO_2 mass fraction decreases gradually from the nozzle to the downstream. The results show an increase in NPR and a decrease in NVR. Moreover, a decrease in the entrainment effect and oxygen content is observed which leads to a low temperature in the afterburning region and an extension in the length of the plume.

B. EFFECT OF AOA ON AFTERBURNING
Generally, the combustion products of propellants, such as H_2, CO, OH, and other unstable components, are fuel-rich.

When the plume interacts with the ambient atmosphere, the air is entrained and reacts with these unstable components to produce stable chemical products, such as CO_2 and H_2O. During this process, a large amount of heat is produced by the chemical reaction, and the temperature of the plume rises sharply. Afterburning occurs as soon as the plume interacts with the environment. Owing to the strong shock wave interaction in the initial region of the plume for an under-expanded jet (see Fig. 2), the oxygen in the environment is gradually mixed with the plume, and afterburning usually exists in the jet region [30] downstream of the plume. To describe the effect of AOA on afterburning, three parameters, T_{peak}, D and L as shown in Fig. 1, are selected to characterize the change in temperature of the afterburning region. Fig.9 shows the curves of aforementioned parameters as a function of AOA for the three cases. Fig. 9(a) shows the relationship between the distance of the maximum temperature offset by the nozzle axis and the AOA. The curve shows approximately linear relationship between offset distance D and AOA with steeper slope for the over-highly under-expanded plume than the moderately and highly under-expanded plume. This means that the under-expanded plume caused by the increase in flight altitude is more sensitive toward the change in AOA. In this case, significant deformation will occur in
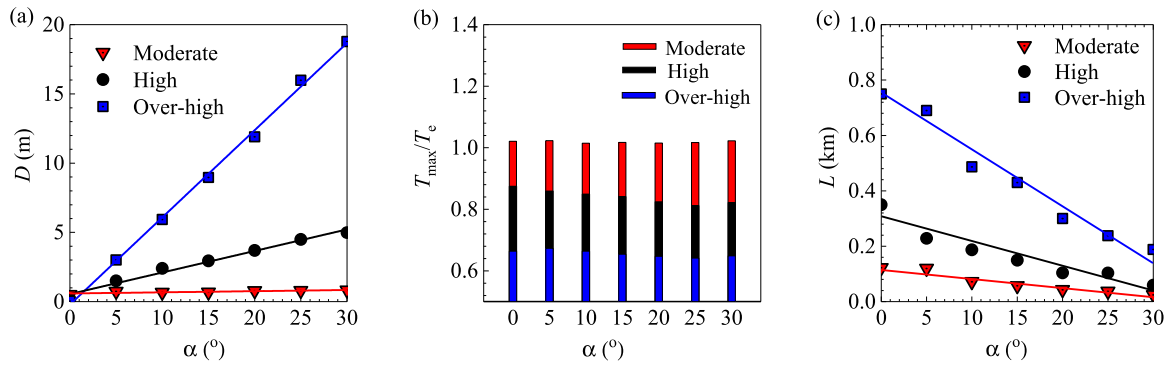
FIGURE 9. Afterburning effect due to AOA variation: (a) corresponding offset distance of peak temperature, (b) peak temperature, and (c) distance between nozzle exit and location at temperature of 1200 K.
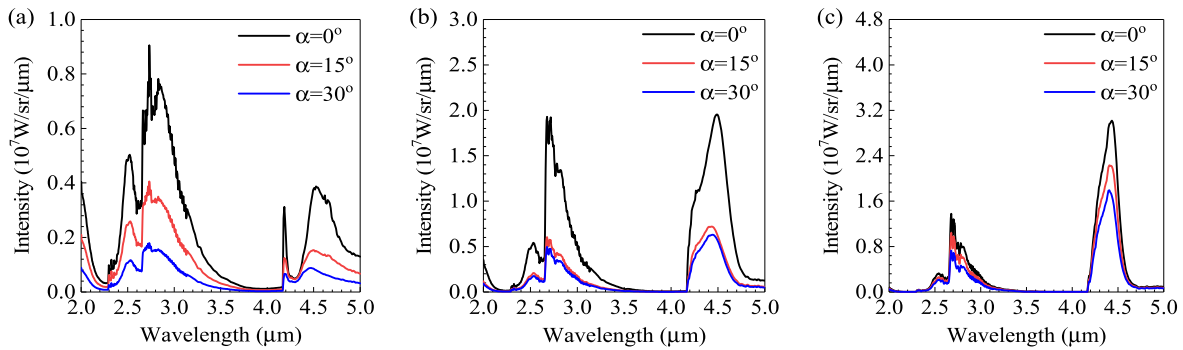

FIGURE 10. Spectra of the plume at three respective AOAs: (a) NPR = 1.27, (b) NPR = 12.5, and (c) NPR = 120.

the high-temperature region compared with the condition of zero AOA.

The variation in the peak temperature with AOA in the afterburning region is shown in Fig. 9(b). The peak temperature is dimensionless with respect to the nozzle temperature. The peak temperature decreases with increasing degree of expansion. For instance, the peak temperature of the over-highly under-expanded plume is 70% of the nozzle exit temperature, while the peak temperature of a moderately under-expanded plume is approximately 10% higher than that of the nozzle exit. It can be considered that the occurrence of AOA cannot significantly change afterburning, at least in the upstream region.

To quantify the effect of AOA on the scale of the afterburning region, a specified temperature of 1200 K is specified. The distance from the specified temperature to the nozzle exit plane as a function of the AOA is presented in Fig. 9(c). It can be seen that the appearance of AOA shortens the length of the afterburning zone. The $L - \alpha$ curve also shows approximately indirect linear relationship. A comparison of the three curves shows that a large AOA can significantly reduce the scale of the high-temperature region at over-highly under-expanded states.

C. EFFECT OF AOA ON IR SIGNATURES
The IR intensity of the exhaust plume depends on several factors including the composition, number density, temperature, observation angle, and atmospheric attenuation. Several

investigations related to the IR characteristics of exhaust plumes at zero AOA have been conducted. Sections V-A and V-B demonstrate that the appearance of AOA has a significant influence on the plume flow, specifically for the distribution and level of temperature and composition. These properties are directly associated with the IR of the plume. An observation angle perpendicular to the axis of the nozzle is considered to analyze the intrinsic radiation signatures of the plume. In addition, self-radiation is used to describe the IR characteristics of the plume without considering the atmospheric attenuation effect along the observation path.

Fig. 10 shows the spectral radiant characteristics of three representative under-expanded plumes in the cases of $\alpha = 0°$, 15°, and 30°. From Fig. 10(a), it can be observed that the spectral radiant intensity of the moderately under-expanded plume with NPR = 1.27 significantly decreases as the AOA increases. An evident absorption peak is observed at wavelength of 4.3 μm. This may be attributed to the effect of CO_2 and temperature distribution in the exhaust plume. Fig. 10(b) shows the spectrum of a highly under-expanded plume with NPR = 12.5. The spectral radiation intensity peaks twice symmetrically at wavelengths of 2.7 μm and 4.3 μm. A highly under-expanded plume with NPR = 120 is shown in Fig. 10(c). It can be seen that the peak radiation intensity of the two bands is opposite to that shown in Fig. 10(a).

The appearance of AOA significantly reduced the spectral peak radiation intensity. The decrease in radiation intensity
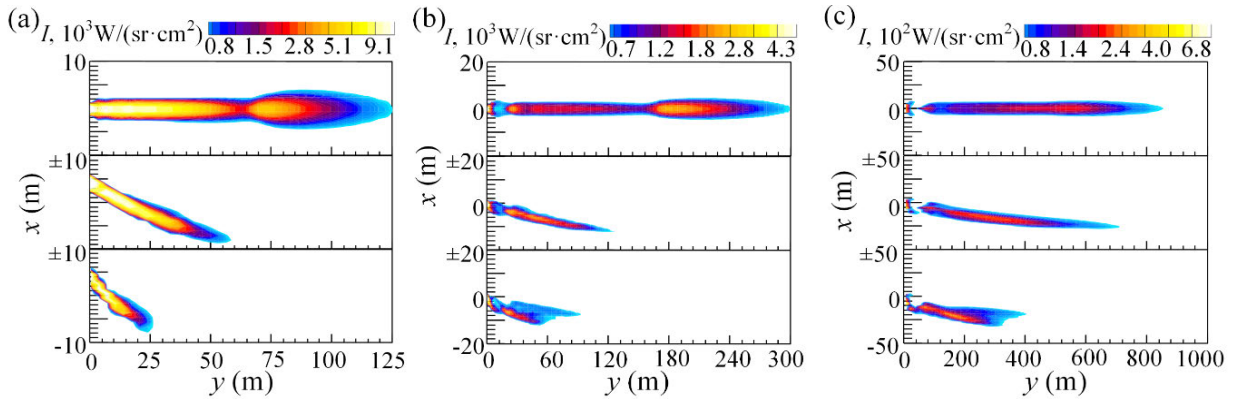
FIGURE 11. Synthetic IR image in the 2.7 μm band: (a) NPR = 1.27, (b) NPR = 12.5, and (c) NPR = 120 from left to right; $\alpha = 0°$, $\alpha = 15°$, and $\alpha = 30°$ from top to bottom.
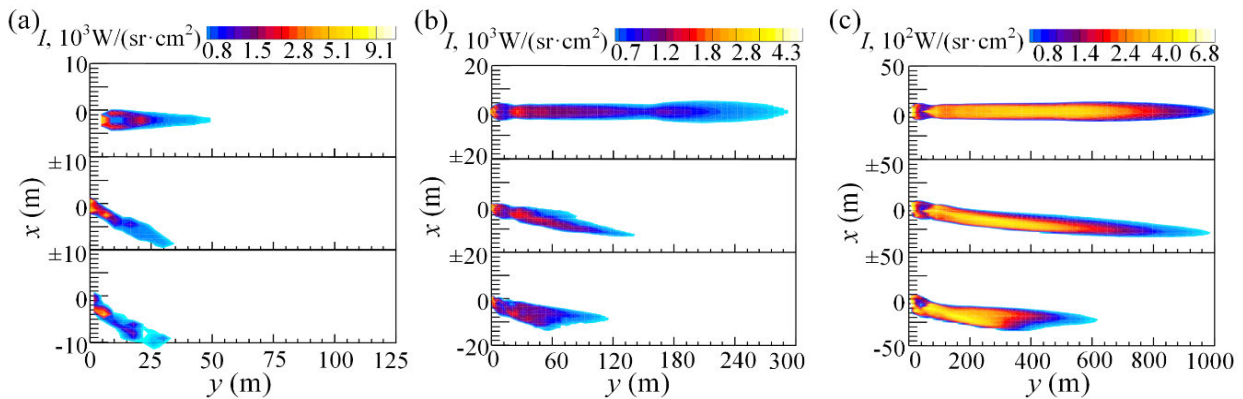

FIGURE 12. Synthetic IR image in the 4.3 μm band: (a) NPR = 1.27, (b) NPR = 12.5, and (c) NPR = 120 from left to right; $\alpha = 0°$, $\alpha = 15°$, and $\alpha = 30°$ from top to bottom.

is not proportional to the increase in AOA, however the rate of decrease becomes gradual for a larger AOA. For instance, the 4.3-μm peak radiation intensity between AOA of 0° to 15° decreases by 63.2% and 12.6% for NPR = 12.5 and NPR = 120, respectively. However, when the AOA increases from 15° to 30°, the peak radiation intensity decreases by 26.3% and 19.6%, respectively. By comparing Figs. 10(a), (b), and (c), the peak spectral intensity at wavelength of 2.7 μm first increases and then decreases with the increase in NPR, while that of 4.3 μm band increases continuously. In addition, the peak spectral intensity at wavelength of 2.7 μm shows a decreasing trend compared with that at 4.3 μm. These differences in radiation intensity are resulted from the combined effect of the species distribution, flow structure, temperature, and LOS path.

Figs. 11 and 12 show the synthetic IR image in bandpass filters of 2.7 μm (2.70 $\pm$ 0.15 μm) and 4.3 μm (4.2 $\pm$ 0.15 μm), respectively. It can be seen that the axial and radial dimensions of the bright region decrease with an increase in the AOA. With increasing flight altitude, the NPR increases and NVR decreases. The bright area in the infrared thermal image, located in the middle and downstream of the plume, becomes larger. This is because the increase in NPR intensifies the under-expanded state of the plume, and the decrease in NVR reduces the mixing of plume in atmosphere,

resulting in the expansion of the afterburning zone. With the appearance of AOA, the region with an evident afterburning effect disappeared. The comparison between Figs. 11 and 12 shows that the radiation intensity and radiation range of the moderately under-expanded plume in the 2.7 μm band are significantly larger than those in the 4.3 μm band. The bright region of the thermal image in the 2.7 μm band of the highly under-expanded plume is located in the afterburning region, while the bright region in 4.3 μm band mainly exists in the upstream of the plume. The radiation intensity of the brightest region of the over-highly under-expanded plume is approximately one order of magnitude lower than that of the other two types of plumes. In addition, the radiation intensity of 2.7 μm band is closer to that of 4.3 μm band, but the radiation intensity of the former is lower than that of the latter in both axial and radial directions.

D. EFFECT OF AOA ON IN-BAND RADIANCE
In addition to the infrared image and spectrum of the plume, the integrated radiation intensity in a specific band is also an important parameter for describing the radiation phenomenon of the rocket exhaust plume, especially for the plume as a point source. Owing to the existence of atmospheric window, the band pass of the infrared detector is generally selected in the range between 3–5 μm. In addition, water vapor and
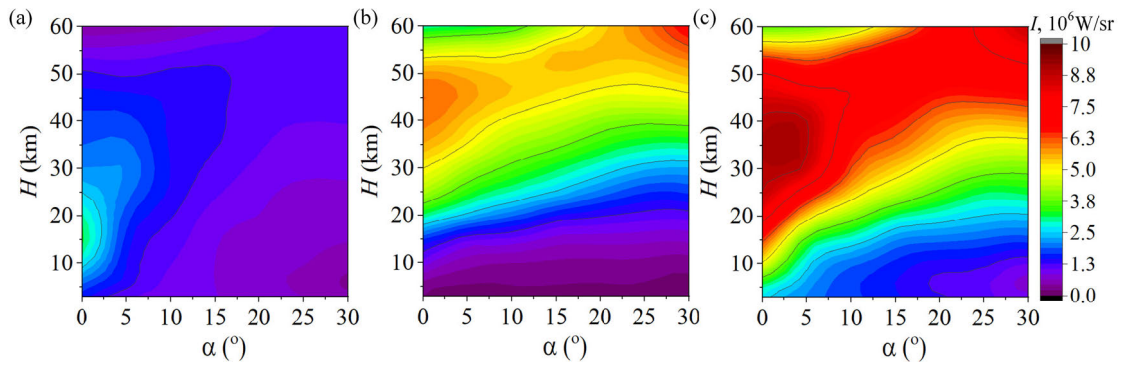
FIGURE 13. Integrated radiation as the function of AOA and flight altitudes: (a) 2.7 μm band, (b) 4.3 μm band, and (c) 3–5 μm band.
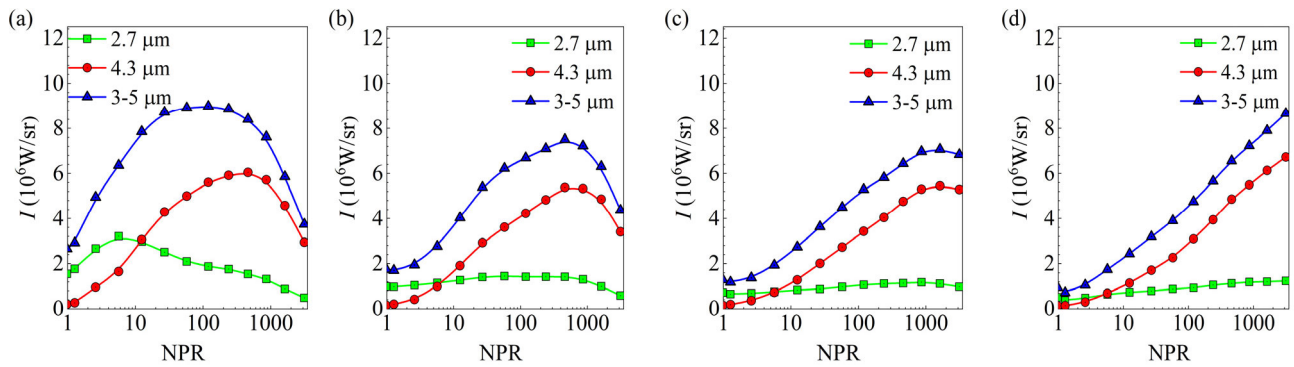

FIGURE 14. Radiance profiles in the 2.7 μm, 4.3 μm and MWIR bands for the case of (a) $\alpha = 0°$, (b) $\alpha = 10°$, (c) $\alpha = 20°$, and (d) $\alpha = 30°$.

carbon dioxide are the main gaseous components of the plume, and their characteristic radiation peaks are in the 2.7 μm and 4.3 μm bands, respectively. Therefore, these two bands are commonly used in engineering applications.

Fig. 13 shows the integrated radiation in the 2.7 μm, 4.3 μm and middle wavelength infrared (MWIR, 3–5 μm) bands as the function of AOA and flight altitudes. By comparing Figs. 13(a) and 13(b), it can be seen that the integrated radiation intensities of 2.7 μm and 4.3 μm bands are considerably different. In the 2.7 μm band, the range of high radiation intensity is small, primarily concentrated in the low altitude and small AOA constrained range. Low radiation intensity occurs in two areas: one is in the range of low altitude and high AOA, and the other is at a high altitude. In the 4.3 μm band, the radiation intensity depends on the flight altitude. The radiation intensity of the high-altitude plume is evidently higher than that of the low-altitude plume. The higher radiation intensity is concentrated in high-altitude large-AOA and medium-altitude small-AOA regions. The results show that a reasonable combination of AOA and flight altitude can potentially reduce the radiation signature of the plume. In the 3–5 μm mid-infrared wave band, the radiation intensity distribution is similar to that of the 4.3 μm band, while the radiation intensity is significantly higher. The high radiation intensity is concentrated in the range of the medium-altitude and small AOA.

To analyze the radiation intensity variation with flight conditions in three typical bands, flight altitude and flight speed
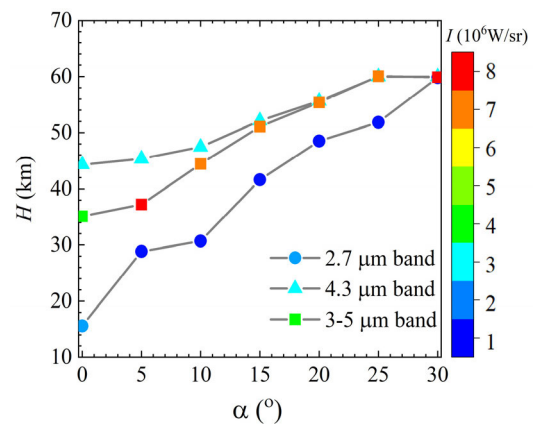

FIGURE 15. Peak in-band radiance with function of AOA and altitude.

are characterized by NPR and NVR, respectively. These two parameters are presented in Fig. 5. A large NPR represents a high altitude. Fig. 14 shows the relationship between the integral intensity in the band and NPR for the four AOA cases of $\alpha = 0°$, $10°$, $20°$, and $30°$. With an increase in AOA, the peak radiation intensity in 4.3 μm band increases and decreases in the 2.7 μm band. The peak value of the 3–5 μm band first decreased and then increased. For the same spectral band, the peak value of the integral radiation intensity curve shifts toward the direction of increasing NPR, and the curve is initially "arched" and gradually becomes smooth with an increase in the AOA. It should be noted that the integral
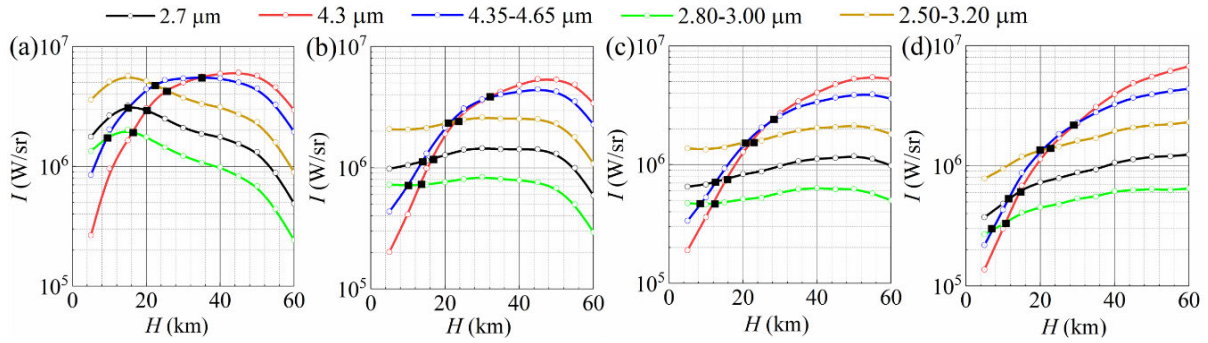
FIGURE 16. In-band radiance profiles with the function of altitudes for different AOA cases: (a) $\alpha = 0°$, (b) $\alpha = 10°$, (c) $\alpha = 20°$, and (d) $\alpha = 30°$.

intensity curves in the 2.7 μm and 4.3 μm bands intersect to form a group of band pairs. With the increasing AOA, the corresponding NPR of the spectral band pair exhibits a slight change. In addition, an increase in AOA significantly enhances the radiation intensity of larger NPRs and decreases the radiation intensity of smaller NPRs. It is evident that the appearance of such band pairs and the formation of characteristic altitudes are significant to plume phenomenology. In Section V-E, the effect of AOA on the band pairs will be analyzed in detail.

Fig.15 shows the relationship among the angle of attack, the peak radiation intensity and the altitude. In this figure, the horizontal ordinate represents AOA, and the vertical ordinate is the altitude where the strongest radiation intensity appears. In addition, the radiation intensity value is represented by a color label. The peak intensity of the 2.7 μm band decreases rapidly in the range of 0°–15°, and decreases slightly in the range of 15°–30°. Its peak range is wide, covering 0–60 km. The peak intensity of the 4.3 μm band increases slightly with the increase in the AOA, which is approximately constant. The characteristic altitude of the peak intensity is more than 40 km. The peak intensity of the 3–5 μm band increases with an increase in the AOA, and its peak value is in a higher altitude range. This is because the radiation intensity of CO_2 in the 4.3 μm band is higher than that in the 2.7 μm band under the combined action of NPR and NVR, which is previously explained in Fig. 10.

E. EFFECT OF AOA ON BAND PAIRS
From Fig. 14, it is observed that the radiation intensity curves of 2.7 μm and 4.3 μm bands can form a group of spectral band pairs, and the corresponding altitude of the spectral band pair is used as the characteristic altitude (H_c), which can be considered as one of the characteristics of a rocket exhaust plume. In this section, five spectral bands, including 2.7 μm, 4.3 μm, 4.35–4.65 μm, 2.80–3.00 μm, and 2.50–3.20 μm bands, are considered. The selected spectral bands are significantly important for infrared detectors and have been reported in Ref. [2].

Fig. 16 shows the radiation intensity distribution curves of the five bands as a function of altitude and the corresponding band pair distribution at four representative AOAs. It can be

seen that the curve distribution of 2.7 μm, 2.80-3.00 μm, and 2.50-3.20 μm bands is significantly different from the other two bands. The intensity of the distribution curves of the three bands are considerably different, however the distribution rules are similar. With an increase in the AOA, the radiation intensity curves present three evident phenomena: (1) the radiation intensity decreases and increases at low and high altitudes, respectively, (2) the peak intensity shifts toward high altitudes, and (3) the radiation intensity distribution curve increases monotonously in the altitude range of 60 km.
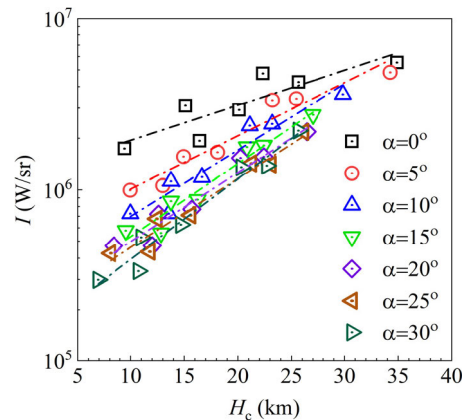

FIGURE 17. Variation of characteristic altitude with AOA change.

To further analyze the variation of the characteristic altitude and radiation intensity with AOA, the distribution of spectral band pairs corresponding to the radiation intensity and characteristic altitude under AOA conditions is shown in Fig. 17. The AOA ranged between 0° to 30° with constant 5° intervals. The best fit-line is used to represent the relationship between intensity and characteristic altitude for different AOAs. It can be seen that the radiation intensity of the band pair decreased with an increase in AOA. The band pair spacing becomes more concentrated and shifts toward low altitudes. In addition, the increase in-band aggregation reduces the coverage of the characteristic altitude and the difference in the radiation intensity of the band pairs. The results imply that the radiation intensity of the plume and degree of feature recognition decrease with an increase in the AOA.

VI. CONCLUSION

In the current study, the influence of AOA on the IR signature of an under-expanded plume was studied using numerical methods. The Atlas-IIA liquid rocket motor with a real trajectory was employed to study the characteristics of the reacting flow field and IR signatures of the plume under moderately, highly, and over-highly expanded states at AOA ranging between 0–30°. The IR characteristic parameters included the spectral radiant intensity, infrared thermal image, integral intensity in the spectral band, and characteristic altitude of the corresponding spectral band pair. We conclude this study as follows:

(1) The appearance of AOA leads to a deformation in the expansion area of the plume, forms a small high-temperature region, and shortens the length of the afterburning zone with an approximately linear relationship.

(2) With an increase in the AOA, the spectral peak radiation intensity decreases and the rate of decrease becomes gradual for a larger AOA. Besides, the axial and radial dimensions of the bright region decrease from the IR image with an evident afterburning effect disappeared.

(3) A reasonable combination of AOA and flight altitude can potentially reduce the radiation signature of the plume. For the same spectral band, the peak value of the integral radiation intensity curve shifts toward the direction of increasing NPR with an increase in the AOA. An increase in AOA significantly enhanced the radiation intensity of larger NPRs and decreased the radiation intensity of smaller NPRs.

(4) The band pair spacing becomes more concentrated and shifts toward low altitudes with an increase in the AOA. The increase in-band aggregation reduces the coverage of the characteristic altitude and the difference in the radiation intensity of the band pairs, which implies that the radiation intensity of the plume and degree of feature recognition decrease with an increase in the AOA.

REFERENCES

[1] O. P. Ely and R. W. Hockenberger, "Rocket exhaust effects on radio frequency transmission," *J. Spacecraft Rockets*, vol. 3, no. 3, pp. 310–314, 1966, doi: 10.2514/3.28445.

[2] F. Simmons, *Rocket Exhaust Plume Phenomenology*, 1th ed. Reston, VA, USA: AIAA, 2000.

[3] C. Paiva and H. Slusher, "Space-based missile exhaust plume sensing: Strategies for DTCI of liquid and solid IRBM systems," in *Space*. Long Beach, CA, USA: AIAA Press, 2005, p. 6820, doi: 10.2514/6.2005-6820.

[4] R. S. Snedeker, "A study of free jet impingement. Part 1. Mean properties of free and impinging jets," *J. Fluid Mech.*, vol. 45, part 2, pp. 281–319, May 1971, doi: 10.1017/S0022112071000053.

[5] R. Castner, A. Elmiligui, and S. Cliff, "Exhaust nozzle plume and shock wave interaction," in *Proc. 51st AIAA Aerosp. Sci. Meeting including New Horizons Forum Aerosp. Expo.*, Jan. 2013, p. 12. [Online]. Available: https://www.researchgate.net/publication/268468292

[6] G. Prigent, "Plume, signal interference and plume signature," in *Solid Rocket Propulsion Technology*. Amsterdam, The Netherlands: Elsevier, 1993, pp. 193–213. [Online]. Available: http://www.sciencedirect.com/science/article/pii/B9780080409993500102

[7] H. J. Li, J. H. Yi, Z. Qin, Z. H. Sun, Y. Xu, C. J. Wang, and F. Q. Zhao, "Influence of afterburning suppression on the combustion of solid propellants: Recent progress and outlook," *J. Phys., Conf. Ser.*, vol. 1507, Mar. 2020, Art. no. 022020. [Online]. Available: https://www.researchgate.net/publication/342774811

[8] K. Kinefuchi, I. Funaki, and T. Abe, "Frequency-dependent FDTD simulation of the interaction of microwaves with rocket-plume," *IEEE Trans. Antennas Propag.*, vol. 58, no. 10, pp. 3282–3288, Oct. 2010, doi: 10.1109/TAP.2010.2055796.

[9] K. Kinefuchi, H. Yamaguchi, M. Minami, K. Okita, and T. Abe, "In-flight S-band telemetry attenuation by ionized solid rocket motor plumes at high altitude," *Acta Astronautica*, vol. 165, pp. 373–381, Dec. 2019, doi: 10.1016/j.actaastro.2019.09.025.

[10] V. Rialland, A. Guy, D. Gueyffier, P. Perez, A. Roblin, and T. Smithson, "Infrared signature modelling of a rocket jet plume–comparison with flight measurements," *J. Phys., Conf. Ser.*, vol. 676, Jan. 2016, Art. no. 012020. [Online]. Available: https://www.researchgate.net/publication/292077860

[11] L. Mengying, L. Shipeng, Z. Liu, Z. Li, and N. Wang, "Numerical simulation on the infrared characteristic of the jet plume of a solid rocket motor," in *Proc. 53rd AIAA/SAE/ASEE Joint Propuls. Conf.*, Jul. 2017, pp. 4861. [Online]. Available: https://www.researchgate.net/publication/318294318

[12] B. Xing-dong, Y. Xi-long, W. Zhen-hua, M. Hong-xia, and L. Dong, "Numerical investigation on flow and radiation characteristics of solid rocket motor plume near the ground," *Procedia Comput. Sci.*, vol. 174, pp. 645–650, Jan. 2020, doi: 10.1016/j.procs.2020.06.137.

[13] Z. Zhou, G. Le, and L. Zhang, "Numerical studies of afterburning on impingement flowfield of the four-engine rockets," *J. Spacecraft Rockets*, vol. 57, no. 6, pp. 1284–1294, May 2020, doi: 10.2514/1.A34672.

[14] I. Rusnak, H. Weiss, R. Eliav, and T. Shima, "Missile guidance with constrained intercept body angle," *IEEE Trans. Aerosp. Electron. Syst.*, vol. 50, no. 2, pp. 1445–1453, Apr. 2014, doi: 10.1109/taes.2014.120100.

[15] A. E. Golubev, A. P. Krishchenko, and N. V. Utkina, "Missile angle of attack tracking using integrator backstepping," *IFAC-PapersOnLine*, vol. 52, no. 16, pp. 724–729, 2019, doi: 10.1016/j.ifacol.2019.12.048.

[16] K. Kennedy, B. Walker, M. DeMagistris, and J. Papp, "Tactical missile exhaust plume at angle of attack," in *Proc. 40th AIAA/ASME/SAE/ASEE Joint Propuls. Conf. Exhib.*, Jul. 2004, p. 3925. [Online]. Available: https://www.researchgate.net/publication/268480679

[17] Q. Niu, Z. He, and S. Dong, "IR radiation characteristics of rocket exhaust plumes under varying motor operating conditions," *Chin. J. Aeronaut.*, vol. 30, no. 3, pp. 1101–1114, Jun. 2017, doi: 10.1016/j.cja.2017.04.003.

[18] Q. Niu, X. Duan, X. Meng, Z. He, and S. Dong, "Numerical analysis of point-source infrared radiation phenomena of rocket exhaust plumes at low and middle altitudes," *Infr. Phys. Technol.*, vol. 99, pp. 28–38, Jun. 2019, doi: 10.1016/j.infrared.2019.04.005.

[19] B. J. McBride and S. Gordon, *Computer Program for Calculation of Complex Chemical Equilibrium Compositions and Applications: II: National Aeronautics and Space Administration, Office of Management*. Washington, DC, USA: NASA, Jul. 1996, doi: 10.1016/S0263-2373(01)00051-2.

[20] H. Mao, D. Fu, and X. Bao, "Engineering method of predicting rocket exhaust plumes at middle and low altitudes," *J. Spacecraft Rockets*, vol. 54, no. 5, pp. 1170–1177, Sep. 2017, doi: 10.2514/1.A33597.

[21] A. Alexeenko, N. Gimelshein, D. Levin, S. Gimelshein, J. Hong, T. Schilling, R. Collins, R. Rao, and G. Candler, "Modeling of radiation in atlas plume-flow," in *Proc. 39th Aerosp. Sci. Meeting Exhib.*, Jan. 2001, p. 355. [Online]. Available: https://www.researchgate.net/publication/269211587

[22] F. Sircilli, S. J. P. Retief, L. B. Magalhaes, L. R. Ribeiro, A. Zanandrea, C. Brink, M. Nascimento, and M. M. Dreyer, "Measurements of a micro gas turbine plume and data reduction for the purpose of infrared signature modeling," *IEEE Trans. Aerosp. Electron. Syst.*, vol. 51, no. 4, pp. 3282–3293, Oct. 2015, doi: 10.1109/TAES.2015.140392.

[23] J. Jia, D. Fu, Z. He, J. Yang, and L. Hu, "Hypersonic aerodynamic interference investigation for a two-stage-to-orbit model," *Acta Astronautica*, vol. 168, pp. 138–145, Mar. 2020, doi: 10.1016/j.actaastro.2019.11.038.

[24] W.-C. Wang, Z.-J. Wei, Q. Zhang, J.-N. Tang, and N.-F. Wang, "Study on infrared signature of solid rocket motor afterburning exhaust plume," in *Proc. 46th AIAA/ASME/SAE/ASEE Joint Propuls. Conf. Exhib.*, Jul. 2010, p. 6847. [Online]. Available: https://www.researchgate.net/publication/277443049

[25] G. Avital, Y. Cohen, L. Gamss, Y. Kanelbaum, J. Macales, B. Trieman, S. Yaniv, M. Lev, J. Stricker, and A. Sternlieb, "Experimental and computational study of infrared emission from underexpanded rocket exhaust plumes," *J. Thermophys. Heat Transf.*, vol. 15, no. 4, pp. 377–383, Oct. 2001, doi: 10.2514/2.6629.

[26] C. B. Ludwig, W. Malkmus, J. Reardon, J. Thomson, and R. Goulard, "Handbook of infrared radiation from combustion gases," NASA, Washington, DC, USA, Tech. Rep. NASA-SP-3080, 1973.

[27] B. Krakow, H. J. Babrov, G. J. Maclay, and A. L. Shabott, "Use of the curtis-godson approximation in calculations of radiant heating by inhomogeneous hot gases," *Appl. Opt.*, vol. 5, no. 11, pp. 1791–1800, Nov. 1966, doi: 10.1364/AO.5.001791.

[28] A. Alexeenko, N. Gimelshein, D. Levin, S. Gimelshein, J. Hong, T. Schilling, R. Collins, R. Rao, and G. Candler, "Modeling of radiation in atlas plume-flow," in *Proc. 39th Aerosp. Sci. Meeting Exhib.*, Jan. 2001, p. 355. [Online]. Available: https://www.researchgate.net/publication/269211587

[29] T. Ozawa, M. B. Garrison, and D. A. Levin, "Accurate molecular and soot infrared radiation model for high-temperature flows," *J. Thermophys. Heat Transf.*, vol. 21, no. 1, pp. 19–27, Jan. 2007, doi: 10.2514/1.19137.

[30] K. Viswanath, D. Levin, K. Brentner, and S. Gimelshein, "Modeling of soot oxidation and prediction of optical radiation in underexpanded plumes," in *Proc. 42nd AIAA Aerosp. Sci. Meeting Exhibit*, Jan. 2004, p. 1350. [Online]. Available: https://www.researchgate.net/publication/268564657

[31] P. Barton, B. Pearce, G. Freeman, A. Tietjen, J. Emery, D. Dawson, J. Wendt, R. Hiers, R. Moyers, and M. Lovern, "Spectral imagery data and mechanisms," in *Proc. 39th Aerosp. Sci. Meeting Exhib.*, Jan. 2001, p. 1121. [Online]. Available: https://www.researchgate.net/publication/269211757

[32] J. Woodroffe, "One-dimensional model for low-altitude rocket exhaust plumes," in *Proc. 13th Aerosp. Sci. Meeting*, Jan. 1975, p. 244. [Online]. Available: https://www.researchgate.net/publication/268455178

WENQIANG GAO was born in Anhui, China. He is a graduate student with the College of Mechatronic Engineering, North University of China. His research interests include numerical simulation of rocket exhaust plume and hypersonic target characteristics.

YIQIANG SUN was born in Hebei, China. He is a doctoral student with the Key Laboratory of Aerospace Thermophysics, MIIT, Harbin Institute of Technology. His research interests include combustion, chemical reaction, and optimization mechanism of rocket engine exhaust plume.

QINGLIN NIU was born in Shanxi, China. He received the Ph.D. degree from Harbin Institute of Technology. He is currently a CFD Simulation Technologist and an Associate Professor at the North University of China. His research interests include high-speed target radiation phenomenology, hypersonic aerodynamics, and engineering thermodynamics.

SHIKUI DONG was born in Jilin, China. He received the M.S. and Ph.D. degrees from Harbin Institute of Technology. He is currently the Head of the Key Laboratory of Aerospace Thermophysics, MIIT, Harbin Institute of Technology. He mainly engaged in target and background optical radiation phenomenology and metamaterials electro-optical thermal coupling mechanism and regulation.

● ● ●